

Investigation of Electronic and Local Structural Changes during Lithium Uptake and Release of Nano-crystalline NiFe₂O₄ by X-ray Absorption Spectroscopy

Dong Zhou^{*a}, Stefan Permien^b, Jatinkumar Rana^a, Markus Krenzel^b, Fu Sun^a, Gerhard Schumacher^a, Wolfgang Bensch^b, John Banhart^{a,c}

^a Helmholtz-Zentrum Berlin für Materialiens und Energie, Hahn-Meitner-Platz 1, 14109 Berlin, Germany

^b Institute of Inorganic Chemistry, University of Kiel, Max-Eyth-Straße 2, 24118 Kiel, Germany

^c Technische Universität Berlin, Materials Science and Technology, Hardenberg straße 36, 10623 Berlin, Germany

Abstract

Nano-crystalline NiFe₂O₄ particles were synthesized and used as active electrode material for a lithium ion battery that showed a high discharge capacity of 1534 mAh g⁻¹ and charge capacity of 1170 mAh g⁻¹ during the 1st cycle. X-ray absorption spectroscopy including XANES and EXAFS were used to investigate electronic and local structural changes of NiFe₂O₄ during the 1st lithiation and de-lithiation process. As lithium is inserted into the structure, tetrahedral site Fe³⁺ ions are reduced to Fe²⁺ and moved from tetrahedral sites to empty octahedral sites, while Ni²⁺ ions are unaffected. As a consequence, the matrix spinel structure collapses and transforms to an intermediate rock-salt monoxide phase. Meanwhile, the inserted Li is partially consumed by the formation of SEI and other side reactions during the conversion reaction. With further lithiation, the monoxide phase is reduced to highly disordered metallic Fe/Ni nanoparticles with a number of nearest neighbors of 6.0(8) and 8.1(4) for Fe and Ni, respectively. During subsequent de-lithiation, the metal particles are individually re-oxidized to Fe₂O₃ and NiO phases instead to the original NiFe₂O₄ spinel phase.

1. Introduction

As the most promising power source for smart phones, laptops, electric vehicles (EVs) and hybrid electric vehicles (HEVs), lithium ion batteries (LIBs) have attracted much attention in past decades. In order to meet the ever-increasing demand for high energy density, high capacity and long service life, various transition metal oxides and compounds (TMOs) have been investigated because of their theoretical capacity based on the conversion reactions that is much higher than that of the commercial lithium intercalation or lithium alloying materials[1-6]. During Li uptake, TMOs are first reduced to extremely small metallic nanoparticles dispersed in a Li₂O matrix. During the subsequent de-lithiation, the metallic particles are re-oxidized. The formal reaction mechanism can be described using the following general equation[1]:



Among these TMOs, iron-based compounds are particularly interesting candidates as they are less expensive and more environmentally friendly than cobalt-containing oxides. Several papers[7-15] have been published on the exploration of iron-based compounds as a substitute for current commercial graphite anode materials, such as Fe₂O₃[7], Fe₃O₄[11], and spinel ferrite MFe₂O₄ (M =Mg, Cu, Co, Ni, Zn and Mn)[8-10, 12-17]. As a member of iron-based compounds, NiFe₂O₄ comes into notice since it displays a high theoretical capacity of 915 mAh g⁻¹[18]. However, TMO electrodes suffer from a rather fast capacity fading within few cycles because of the formation of an insulating polymeric layer around the particles and poor integrity caused by the marked volume changes upon cycling[9, 19, 20]. Various strategies have been used to improve the electrochemical behavior of NiFe₂O₄. NuLi *et al.*[7] prepared nano-crystalline NiFe₂O₄ ferrite thin films by an electrochemical route, which delivered a reversible capacity of 450–460 mAh g⁻¹ at 10 μAcm⁻² and more than 75% reversible capacity still remaining up to 100 cycles. Ding et al.[21] synthesized a hierarchically nanostructured NiFe₂O₄/C composite

which showed a high specific capacity of 780 mAh g⁻¹ after 40 cycles. Cherian *et al.*[22] reported NiFe₂O₄ nanofibers with a reversible capacity of 1000 mAh g⁻¹ after 100 cycles.

Though the conversion reaction (1) of simple monoxides (CoO, CuO, FeO or NiO)[1] is thermodynamically favorable and has been widely investigated by *ex-situ/in-situ* X-ray diffraction (XRD), transmission electron microscopy (TEM), X-ray photoelectron spectroscopy (XPS) and Mössbauer spectroscopy during discharging and charging, the reaction is still not well understood due to the intriguing nature of Li₂O and ultrafine metal particles and limitations for the above mentioned analytic techniques. For example, the highly disordered metallic particles formed during discharge cannot be detected by XRD because they are presumably smaller than the coherence length of the corresponding X-rays[1]. Sample preparation for TEM is laborious and it is easy to introduce artifacts which affect the results. XPS is sensitive to the sample surface and cannot provide information about bulk properties. A deeper understanding of the reactions for TMOs occurring during lithiation and delithiation is crucially important for the search for new high-performance electrode materials. X-ray absorption spectroscopy (XAS), a unique elementary selective technique, is a very useful tool for clarifying the changes in oxidation state and local environment of each absorbing atom of TMO electrodes since it does not require long-range order, and provides a chance to get a deeper insight into individual reaction steps of the conversion reaction.

In the study presented here, we investigated electrical and local structural changes in nano-crystalline NiFe₂O₄ anode material by using X-ray absorption near edge structure (XANES) and extend X-ray absorption fine structure (EXAFS) in order to establish and elucidate a more detailed conversion reaction mechanism upon charge and discharge.

2. Experimental

2.1 Synthesis

NiFe₂O₄ nanoparticles were synthesized by mixing 5 mmol Ni(NO₃)₂·6H₂O (97 %, Merck), 10 mmol Fe(NO₃)₃·9H₂O (98 %, Riedel-de Haen), 3 mL Ethylenglycol (99 %, Merck Millipore) and 15 mmol succinic acid (99 %, Merck) in a Fritsch Pulverisette ball mill for 2 h with 15 mm agate balls at 500 rpm in air. The viscous product was decomposed at 400 °C in a pre-heated oven for 3 h.

2.2 Materials characterization and electrochemical Li insertion

XRD patterns of pristine NiFe₂O₄ were recorded on a X'PERT PRO (P-analytical) instrument equipped with a PIXcel detector using Cu K_α radiation. EDX spectra were obtained using a Philips ESEM XL 30 equipped with an EDX detector from EDAX company. TEM investigations were performed in a Tecnai F30 G²-STwin microscope operated at 300 kV with a field emission gun cathode and a Si/Li detector (EDAX). The NiFe₂O₄ nanoparticles were suspended in n-butanol and dropped on a holey-carbon copper grid for TEM. For electrochemical characterization, 70 wt% NiFe₂O₄ were mixed with 20 wt% carbon (Super C65 Timcal, Suisse) and 10 wt% sodium carboxy methylcellulose (Sigma-Aldrich, Germany) as a binder. The compounds were mixed with distilled water to a viscous slurry, painted on copper foil and dried over night at room temperature. Afterwards, 10 mm discs were cut each containing ~2-3.5 mg of active material. NiFe₂O₄ nanoparticles were used as the anode in a Swagelok-type test cell, using lithium metal as the cathode, glass fiber filter discs (Whatman, UK) as the separator, and a solution of 1 M LiPF₆ in an 1:1 ethylene carbonate-dimethyl carbonate mixture (BASF, Germany) as the electrolyte. Test cells were assembled in an MBraun argon-filled glove box (<1 ppm O₂, <1 ppm H₂O) and discharged with a C/10 rate (theoretical capacity 933 mAh g⁻¹). Galvanostatic charge-discharge experiments were performed with a Material Mates 510 DC until the desired formal composition or the cell potential were reached. The cells were opened under argon atmosphere and active material was scraped off the Cu foil and mixed with graphite (Sigma-Aldrich, 99.99%) in an agate mortar. For the XAS measurements, a pellet with about 18wt% electrode material and 82 wt% graphite were pressed and protected with adhesive Kapton tape. The pellets were transferred to the beam line in an air tight glass container.

Ex-situ XAS analysis at the Fe and Ni K-edge was performed in transmission mode at the KMC-2 beamline of the synchrotron BESSY at Helmholtz-Zentrum Berlin, Germany. This beamline is equipped with a graded Si-Ge (111) double -crystal monochromator. About 65% of the maximum possible intensity of the beam is transmitted through the sample during the measurement. The energy was calibrated using Ni or Fe foil. The data were processed by using the software ATHENA and ARTEMIS of the package IFEFFIT as reported in the literature[23, 24]. Each spectrum was energy-calibrated with respect to the first peak in their corresponding reference metal foil derivative spectrum. The normalized EXAFS signal in k space was multiplied by k^3 in order to obtain a good signal at high k values because of the damping effect and Fourier transformed in R space without phase shift correction. The model for each fitting was generated based on the known crystal structure by performing ab initio calculations using the code FEFF8[25]. Change in the bond length ΔR was calculated by $\Delta R = \alpha_{\text{fit}} \times R_{\text{theory}}$, where α_{fit} is the refined fractional change for each coordination shell. The Debye-Waller factor σ^2 is also given for each coordination shell depending on the mass of the backscattering atoms and their distance from the absorber. Multiple scattering paths were included but the fitting parameters were constrained to those of single scattering paths. The statistical quality of each EXAFS fit was evaluated based on its R-factor.

3. Results and Discussion

Fig. 1 shows the XRD pattern of as-synthesized NiFe_2O_4 together with the calculated diagram. The XRD pattern can be indexed with the $Fd\bar{3}m$ space group in an inverse cubic spinel structure. The lattice parameter and volume-weighted average particle size obtained by Rietveld refinement of the XRD data are $a = 8.3469(5)$ Å and $D = 12(1)$ nm, respectively.

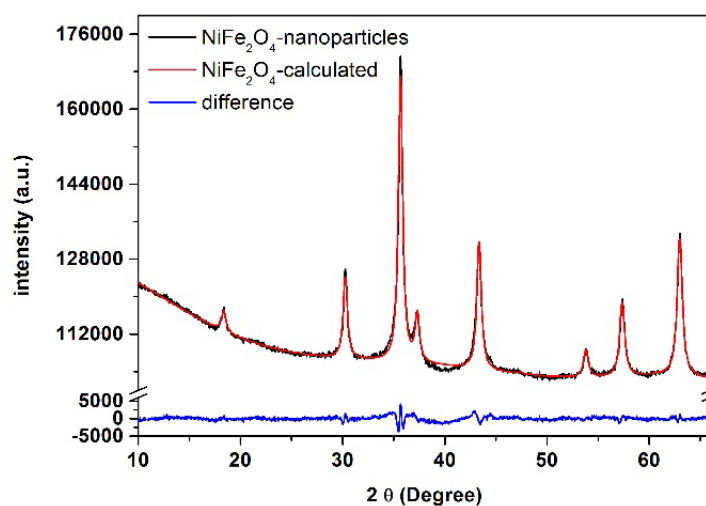


Fig. 1 XRD pattern of the prepared nano-particles. The calculated X-ray pattern of NiFe_2O_4 is shown for comparison.

The morphology of pristine NiFe_2O_4 powder was examined by TEM, and is shown in Fig. 2(a). As can be seen, the nanoparticles agglomerate with each other showing typical sizes around 10 nm. The SAED pattern in Fig. 2(b) verifies the spinel structure of NiFe_2O_4 .

The results of cyclic voltammetry (CV) carried out at a scan rate of 0.05 mVs^{-1} for 3 cycles and discharge/charge voltage profiles for the 1st cycle of the NiFe_2O_4 anodes are given in Fig. 3(a) and (b), respectively. Significant differences can be observed in Fig. 3(a) between the first and subsequent cycles, which is consistent with the results reported in the literature[26]. The sharp cathodic peak at around 0.45V corresponds to the reduction of nickel and iron ions to the metallic state during the first discharge. The hardly resolved two cathodic peaks at around 1.65V and 1.9V are due to the oxidation of metallic nanoparticles during the first charge process. The initial spinel structure does not seem to be restored after the first cycle. A specific capacity of 1534 mAh g^{-1} is attained as the cell is discharged to 0.1V, while it delivers a capacity of 1170 mAh g^{-1} as it is charged to 3.0V. The six circles marked in blue in the voltage profiles (Fig. 3(b)) represent the six different states studied by X-

ray absorption spectroscopy (including XANES and EXAFS), i.e., pristine state, 0.95V, 0.76V, 0.75V and 0.1V during the 1st lithiation and 3.0V during charge after the 1st discharge, respectively.

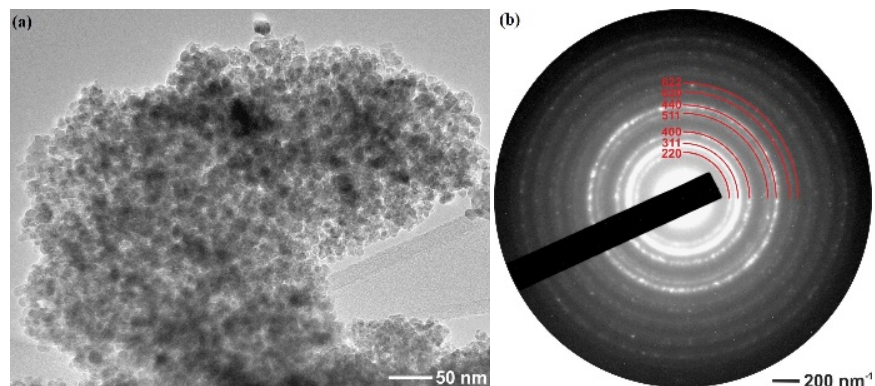


Fig. 2 (a)TEM bright-field image of a pristine NiFe₂O₄ sample; (b) corresponding SAED pattern.

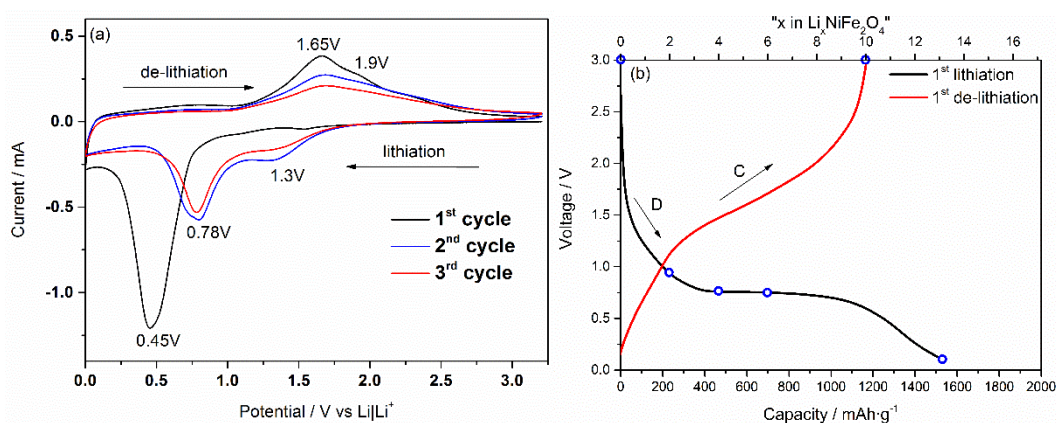


Fig. 3 (a) Cyclic voltammetry of NiFe₂O₄ anodes and (b) Voltage vs. specific capacity profiles of NiFe₂O₄ for the 1st discharge(D)/charge(C) cycle measured at constant current and using charge and discharge rates of 0.1C (1C = 933 mAh g⁻¹). Arrows mark progressing time, circles the states selected for XAS measurements.

3.1 XANES

Fig. 4(a) shows the normalized Fe K-edge XANES spectra of NiFe₂O₄ at various states of the 1st cycle. The K-edge XANES spectra of 3d transition metals are usually characterized by a threshold energy, a pre-edge and a main edge, which provide information about the oxidation state and site symmetry of the absorbing atom. In principle, a small pre-edge peak which is due to the dipole-forbidden 1s → 3d transition and a main peak which is caused by the 1s → 4p transition can be observed for 3d TMOs. The weak pre-edge peak can only be observed in the presence of 3d → 4p orbital mixing or direct quadrupolar coupling. Since the outer p-orbitals are more sensitive to electronic changes, the average valence state of the absorbing atom can be estimated from the position of the main absorption edge with respect to reference materials[27]. As the valence state of the central absorbing atom decreases, all the main features shift to lower energies and vice versa. From Fig. 4(a) it can be seen that the pre-edge and main edge of the pristine NiFe₂O₄ sample are close to that of the Fe₂O₃ reference compound. Fe ions of pristine NiFe₂O₄ therefore appear to have a formal oxidation state of +3. After the uptake of 6 lithium ions into the NiFe₂O₄ electrode (0.75V, 1st D), the main edge shifts close to that of the FeO compound without a change in shape, pointing at the reduction of Fe³⁺ ions to Fe²⁺ ions. The only explanation for this would be that 4 of the 6 Li are consumed by the SEI formation and other side reactions. With further discharge to 0.1V, the energy position and shape of the main edge seem to be identical to that of the reference Fe metal, suggesting the reduction of iron ions to the metallic state. During the subsequent charge to 3.0V, the pre-edge peak shows up and the main edge shifts to higher energy, reflecting the oxidation of metallic Fe during Li release.

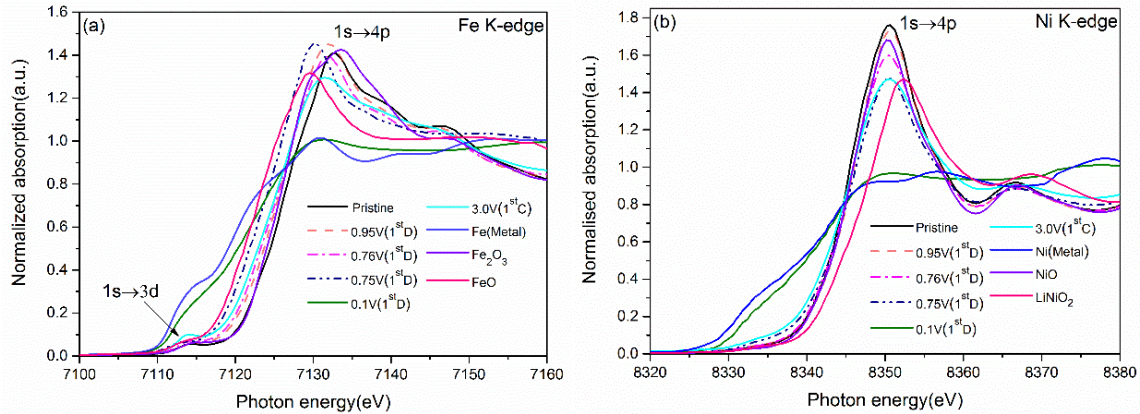


Fig. 4 Normalized absorption spectra at the (a) Fe and (b) Ni K-edge of NiFe_2O_4 in various states during 1st discharge and charge. Notations: 0.95V (1st D) means discharge of the cell to 0.95V in the first cycle, and so on. 3.0V (1st C) means charge the cell to 3.0V after the cell has been discharged to 0.1V in first cycle.

Unlike the Fe K-edge XANES spectra, a very weak pre-edge peak can be observed at the Ni K-edge of the pristine state (Fig. 4(b)) because of the dipole-forbidden $1s \rightarrow 3d$ transition in a centrosymmetric field, which is expected since Ni atoms have an octahedral coordination in the inverse spinel structure. The main absorption edge stays at the same energy position (around 8351 eV) as NiO oxide and remains there until the cell has been discharged to 0.75V. This indicates that most Ni^{2+} ions are not reduced at this voltage because of the SEI formation and other side reactions, which is also in good agreement with the results of Fe. As the cell is further discharged down to 0.1V, similar to Fe, the absorption line becomes smooth and overlaps with that of the reference Ni metal, suggesting the reduction of Ni^{2+} ions to metallic nickel. As the cell is charged to 3.0V, the main absorption edge moves back to 8351 eV along with a steep white line. These changes can be interpreted by the re-oxidization of metallic Ni to Ni^{2+} ions during the charge process.

3.2 EXAFS

Fig. 5(a) represents the k^3 -weighted EXAFS $\chi(k)$ signals at the Fe K-edge of NiFe_2O_4 , while their corresponding Fourier transforms are shown in Figure 5(b). As can be seen in Fig. 5(a), the $\chi(k)$ signal shifts slightly to lower k values and varies from $k \approx 9 \text{ \AA}^{-1}$ as the cell is discharged to 0.95V. Then the signal gradually fades out with increasing insertion of Li^+ . With further discharge to 0.1V, clear differences in the EXAFS spectrum can be seen compared to that of the pristine NiFe_2O_4 sample and the signal does not recover during the following charge to 3.0V. In the corresponding Fourier transforms in Fig. 5(b), the spectrum of pristine NiFe_2O_4 is in good agreement with that of the inverse spinel structure ($[\text{Fe}^{3+}]_{\text{tetra}}[\text{Ni}^{2+}\text{Fe}^{3+}]_{\text{octa}}\text{O}_4$), where the first-shell peak is due to backscattering from oxygen anions around tetrahedral Fe sites and octahedral Fe/Ni sites[28]. In contrast, the peaks at $\sim 2.8 \text{ \AA}$ and $\sim 3.2 \text{ \AA}$ are arisen from the scattering from metals around the octahedral site and both octahedral and tetrahedral sites respectively. Interestingly, as the cell is discharged to 0.95V, the intensity of $\text{Fe-TM}_{\text{tetra/octa}}$ peak located at $\sim 3.2 \text{ \AA}$ markedly decreases. This may be caused by the movement of the reduced Fe^{2+} ions from tetrahedral to empty octahedral sites due to the strong repulsive interaction between inserted lithium ions and transition metal cations in the structure, which has also been observed by other groups[29, 30]. In the study of structural changes of lithiated magnetite $\text{Li}_x\text{Fe}_3\text{O}_4$, Thackeray *et al.*[29] found that inserted lithium ions first occupy one-half of the interstitial octahedral sites (16c) and then cooperatively displace the tetrahedral site iron ions into the empty octahedral sites at 16c so that the partially ordered rock-salt type structure $(\text{LiFe})_{16c}[\text{Fe}_2]_{16d}\text{O}_4$ is produced when $x=1.0$. They concluded that Fe_3O_4 undergoes a structural phase transition to a FeO-type rock-salt phase upon lithiation to $\text{Li}_2\text{Fe}_3\text{O}_4$.

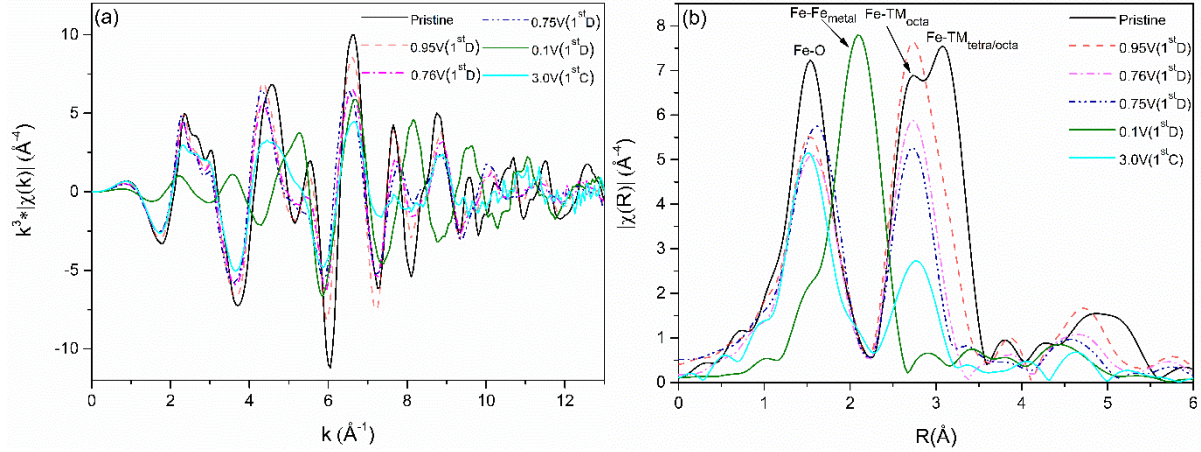


Fig. 5 (a) k^3 -weighted EXAFS $\chi(k)$ signals and, (b) their Fourier transforms at the Fe K-edge of NiFe_2O_4 in various states during discharge and charge. Notations: Fe-O corresponds to oxygen atoms in the 1st shell around Fe absorbers, Fe-TM_{octa} corresponds to Fe/Ni atoms sited on the octahedral situated in the 2nd shell around Fe absorbers, and Fe-TM_{tetra/octa} corresponds to Fe/Ni atoms sited on the octahedral situated and Fe atoms situated on the tetrahedral site in the 3rd shell around Fe absorbers in the inverse spinel structure. Fe-Fe_{metal} corresponds to Fe atoms in the 1st shell around Fe absorbers in metallic iron. Discrete data points are presented by lines for the sake of clarity.

Upon further discharge to 0.75V, no new peak can be observed in Fig. 5(b). Combining the results from EXAFS and XANES measurements, it seems that the phase transition from spinel to rock-salt monoxide is still underway at this state (0.75V, 1stD). Possibly, the inserted lithium ions are partially consumed by the formation of solid electrolyte interface (SEI) around electrode particles instead of reacting with the active electrode material itself, which has been observed in CoO anode materials[31]. As the cell is discharged to 0.1V, only one intense Fe-Fe_{metal} peak ($\sim 2.2\text{\AA}$) can be seen, which is consistent with that of the calculated Fe K-edge EXAFS spectrum of highly disordered Fe nanocrystal (size $\sim 3\text{nm}$) reported by Sobczak *et al.*[32]. The loss of long-range order of the newly formed metallic iron nanoparticles suggests the existence of pronounced disorder in the structure. During subsequent charge up to 3.0V, the Fe-Fe_{metal} peak is replaced by the Fe-O peak, manifesting the oxidation of metallic iron during de-lithiation. Guo *et al.*[9] pointed out that in the ZnFe_2O_4 electrode, Fe and Li-Zn alloy were formed as the cell was deeply discharged and Fe_2O_3 was formed after recharging the battery. This was derived from HRTEM and first-principle calculations.

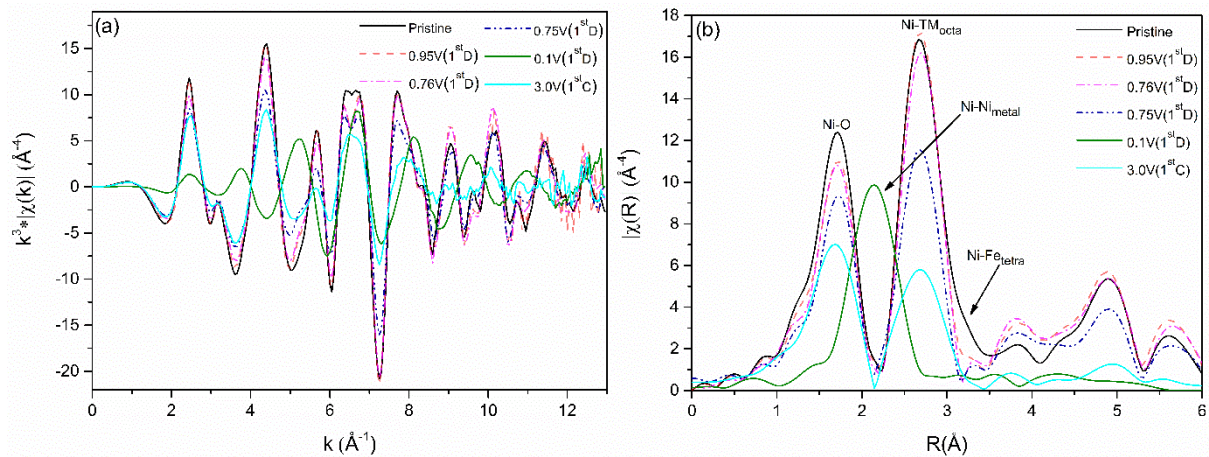


Fig. 6 (a) k^3 -weighted EXAFS $\chi(k)$ signals and, (b) their Fourier transforms at the Ni K-edge of NiFe_2O_4 in various states during discharge and charge. Notations: Ni-O corresponds to oxygen atoms in the 1st shell around Ni absorbers, Ni-TM_{octa} corresponds to Fe/Ni atoms situated on the octahedral site in the 2nd shell around Ni absorbers, and Ni-Fe_{tetra} corresponds to Fe atoms situated on the tetrahedral site in the 3rd shell around Ni absorbers in the inverse spinel structure. Ni-Ni_{metal} corresponds to Ni atoms in the 1st shell around Ni absorbers in metallic nickel. Discrete data points are represented by lines for the sake of clarity.

Fig. 6(a) shows the k^3 -weighted EXAFS $\chi(k)$ signals at the Ni K-edge of NiFe_2O_4 . Similar to Fe, the signals in k space are increasingly damped as the cell is discharged from the pristine state to 0.75V. With further discharge to 0.1V and the following charge to 3.0V, the intensity and shape of the $\chi(k)$ signals vary markedly compared to the pristine sample. More pronounced changes can be observed in their corresponding Fourier transforms in Fig. 6(b). At the beginning of lithiation, the small Ni- Fe_{tetra} shoulder which corresponds to the contribution of Fe atoms on tetrahedral sites, first disappear, followed by a systematic reduction of the amplitude of all peaks during further discharge to 0.75V. At the end of discharge, only one single Ni- Ni_{metal} peak located at $\sim 2.1\text{\AA}$ can be observed, suggesting the formation of metallic nickel nanoparticles. Upon subsequent charge to 3.0V, the Ni- Ni_{metal} peak vanishes and the Ni-O peak reappears. Therefore, it can be concluded that the newly formed metallic nickel is oxidized during the release of lithium ions in the charge process.

In order to get more quantitative information about structural changes during lithiation and de-lithiation process, the EXAFS data of the most important samples were fitted at various states including few reference materials. Since Fe and Ni are close to each other in the periodic table of the elements and, therefore, have similar backscattering amplitudes, only Fe backscatters are considered at Fe K-edge, and only Ni backscatters are considered at Ni K-edge. The fits are shown in Fig. 7 for the Fe K-edge and in Fig. 8 for the Ni K-edge respectively. The fit parameters for each EXAFS data set are listed in Table S1-S12 in the SI. The data is in good agreement with the model for all states as all the R-factors of the fits are less than 0.02.

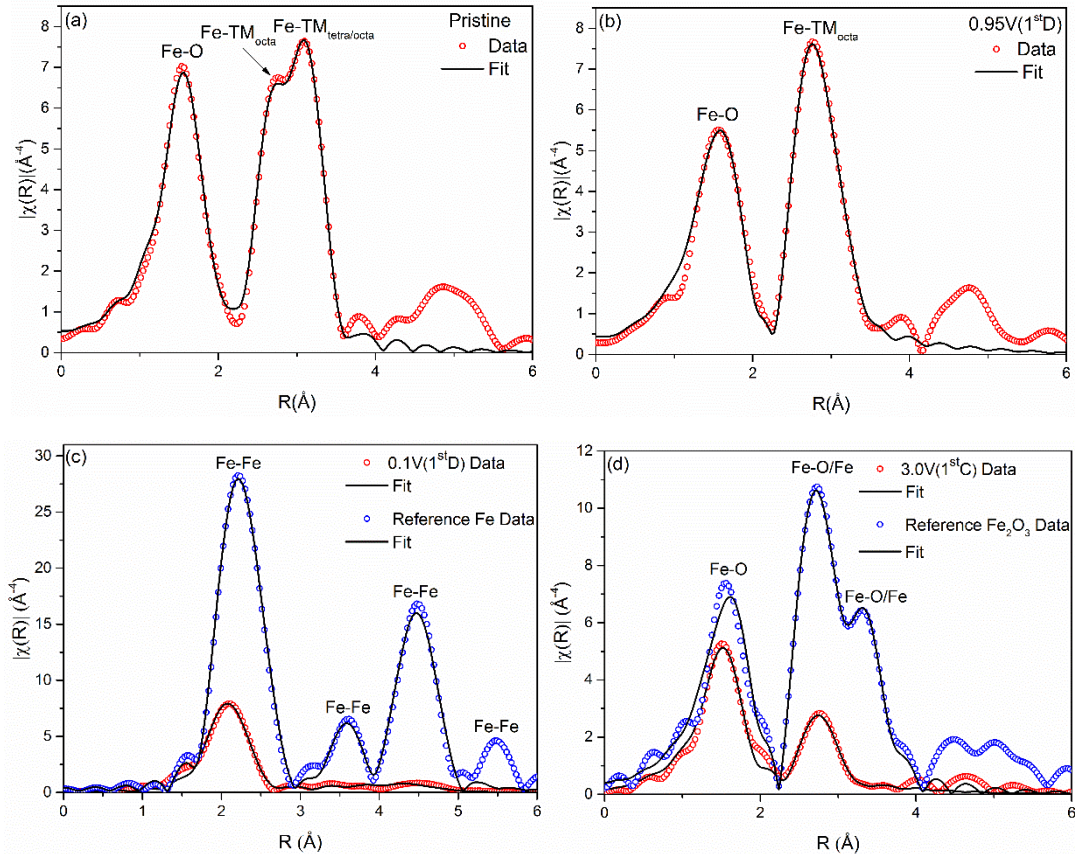


Fig. 7 EXAFS fits to the data measured at the Fe K-edge of NiFe_2O_4 in various states during charge and discharge compared to reference compounds.

The EXAFS data at both the Fe and Ni K-edge of the pristine sample is fitted well up to $\sim 4\text{\AA}$ with a totally inverted spinel structure[33] ($[\text{Fe}^{3+}]_{\text{tetra}}[\text{Ni}^{2+}\text{Fe}^{3+}]_{\text{octa}}\text{O}_4$), where Ni^{2+} ions occupy octahedral sites and Fe^{3+} ions are equally distributed between tetrahedral and octahedral sites. As the cell is discharged to 0.95 V corresponding to 2 lithium ions inserted per formula unit, all the Fe^{3+} ions should be reduced to Fe^{2+} ions and form a rock-salt structure monoxide according to the charge compensation mechanism without consideration of the SEI formation

in the electrode. However, in the NiFe_2O_4 electrode, Fe shows a mixed valence state between +2 and +3 at this voltage, which evidences the consumption of lithium ions due to SEI formation. An intermediate model structure $[\text{Ni}^{2+}\text{Fe}^{3+}]_{\text{octa}}[\text{LiFe}^{2+}]_{\text{octa}}\text{O}_4$ is proposed to fit the data collected at 0.95V because of the movement of tetrahedral site Fe cations during lithiation. The data is fitted well with the proposed model structure. Table. 1 illustrates the refined average bond length of the 1st and 2nd coordination shells around Fe and Ni cations as derived from the fits. A clear increase can be observed around Fe cations in two coordination shells, which is caused by the reduction of Fe^{3+} to Fe^{2+} and migration of Fe^{2+} ions. On the contrary, the refined bond length R_{mean} for both Ni-O and Ni-TM shells around Ni cations are almost constant, suggesting that Ni ions are nearly unaffected as the cell is discharged to 0.95V. Unfortunately, with further discharge to 0.75V, the EXAFS data cannot be fitted at both the Fe and Ni K-edges because of the complexity of the conversion reactions that have taken place in the electrode. The XAS signal at this voltage may represent a mixture of several metastable phases. Therefore, it is hard to find out the proper fraction for each structure in the mixture of phases to fit the data.

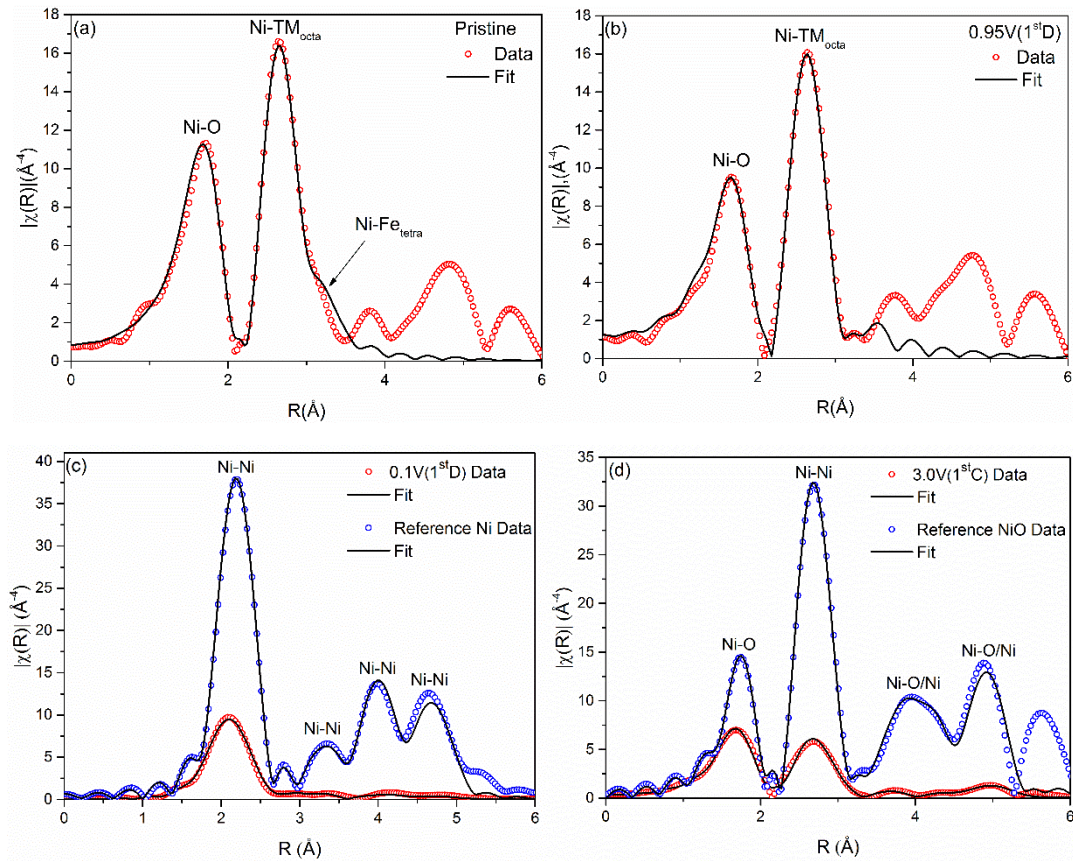


Fig. 8 EXAFS fits to the data measured at the Ni K-edge of NiFe_2O_4 in various states during charge and discharge and relative reference compounds.

For transition metal oxides in the spinel structure, it is widely accepted that nano-sized metallic products form as the cell is discharged and then re-oxidized during subsequent charge[1]. In NiFe_2O_4 , the fitting results are in good agreement with the formation of nano-sized metallic clusters. We find that the spinel NiFe_2O_4 is reduced to metallic iron and nickel as the cell is deeply discharged and then re-oxidized to Fe_2O_3 and NiO during the following charge. However, there is one important observation: Compared with the reference materials, the amplitude of each peak is reduced in R space for the newly formed metallic nanoparticles and their corresponding oxides as shown in Fig. 7(c, d) and Fig. 8(c, d), respectively. The amplitude of the EXAFS signal for each coordination shell in the structure is mainly affected by two factors: (1) the product of $S_o^2 \times N$, where S_o^2 is the amplitude reduction factor and N is the number of coordinating atoms in that shell; (2) The Debye-Waller factor

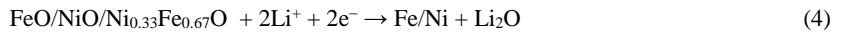
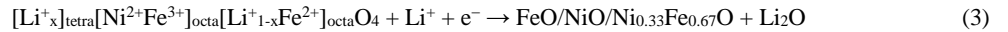
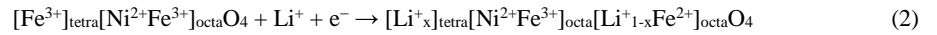
σ^2 which represents static and thermal disorder for a given shell. Therefore, it is crucial not to vary S_o^2 and N for any shell simultaneously in one fit. Since S_o^2 is transferable between compounds with the same absorbing atom–ligand combination, it can be constrained to the value obtained from reference compounds. Thus, N and σ^2 can be refined for each shell.

Table 1. Refined average bond length of 1st and 2nd coordination shells around Fe and Ni atoms of NiFe₂O₄ in the pristine state and after discharge to 0.95V.

Sample name	Fe-O (1 st shell)	Fe-TM (2 nd shell)	Ni-O (1 st shell)	Ni-TM (2 nd shell)
Pristine	1.915(8)	2.866(8)	1.930(6)	2.887(4)
0.95V(1 st D)	1.982(8)	2.956(9)	1.919(10)	2.883(5)

According to the refined number of nearest neighbors of absorbing Fe and Ni atoms for the 1st coordination shell as the cell is discharged to 0.1V, the coordination number for metallic Fe is reduced to 6.0(8) (for bcc α -iron this should be 8) and for metallic Ni to 8.1(4) (for fcc nickel this should be 12). The reduced coordination number N suggests that the metal particles formed during the discharge process are quite small since N can play a significant role in the signal amplitude suppression only when the particle size is smaller than 5 nm according to a calculation based on the crystallite size and crystallite structure[34]. Similar results are also reported for NiCo₂O₄ anode materials[35]. As the NiCo₂O₄ electrode is fully discharged to 0V, it gives a coordination number N~5 for Co and N~4 for Ni, respectively, without concerning the effect of disorder to the signal[35]. In principal, the Debye-Waller factor σ^2 will increase as the particle size decreases in nano-crystalline materials because of surface effects. At the surface, the coordination number is reduced compared to the bulk.

Based on the electrochemical and structural analysis of the NiFe₂O₄ anode during the 1st lithiation and de-lithiation presented above, a new lithium storage mechanism of NiFe₂O₄ is proposed without taking into account the possible formation of SEI. At the beginning of lithiation, lithium ions can enter both empty tetrahedral or octahedral sites in the spinel structure. However because of the strong repulsive interactions between Li⁺ and Fe³⁺ ions, tetrahedral site Fe³⁺ ions are reduced to Fe²⁺ and forced to move to the empty octahedral sites, c.f. Eq.(2). This structural relaxation has also been reported in many other spinel ferrites such as MgFe₂O₄[14], ZnFe₂O₄[20], MnFe₂O₄[36] and Fe₃O₄[37]. With further lithiation (uptake of up to 2 lithium per formula unit), the lithiated phase starts to decompose into Li₂O and rock-salt monoxide phases, c.f. Eq. (3). Unfortunately, we cannot determine the accurate chemical composition of the newly formed rock-salt phase because of the similar backscattering powers of Fe and Ni atoms. A simple Ni_{0.33}Fe_{0.67}O phase or a mixture of FeO and NiO phases are presumably formed at this voltage. As the cell is discharged to 0.1V, the monoxides are further reduced to metallic particles dispersed in a Li₂O matrix, c.f. Eq. (4). A total of 8 lithium ions are reacted with per formula unit NiFe₂O₄ in the course of 1st discharge.



During de-lithiation, metallic iron and nickel are oxidized to Fe₂O₃ and NiO, respectively, corresponding to 8 lithium ions that can be delivered according to Eqs. (5) and (6).



4. Conclusion

X-ray absorption spectroscopy was used to investigate electronic and local structural modifications around Fe and Ni atoms in the inverse spinel ferrite NiFe_2O_4 anode material at various states of discharge and charge during the 1st cycle. Although Fe and Ni absorbers behave differently during cycling, both of them are reduced to the metallic state during lithiation and re-oxidized during subsequent de-lithiation as clearly observed by both XANES and EXAFS. At the onset of discharge to 0.95V, tetrahedral site Fe^{3+} ions are first reduced to Fe^{2+} and then displaced to octahedral sites due to the strong repulsive interactions between inserted Li^+ ions and Fe^{2+} ions. This corresponds to the uptake of 2 lithium ions per unit formula. Unlike for Fe, no clear changes can be observed for Ni. Upon further lithiation, the spinel structure collapses and transforms to a rock-salt monoxide phase. However no signal from metallic iron or nickel can be observed as 6 lithium are inserted per formula unit at 0.75V, which indicates that the inserted lithium ions are possibly partially consumed due to the formation of SEI and other side reactions during the phase transition from spinel to rock-salt monoxide. Finally, the monoxide is reduced to metallic iron and nickel nanoparticles. The refined EXAFS results reveal that the metallic iron and nickel particles are highly disordered with a number of nearest neighbors of 6.0(8) and 8.1(4) for Fe and Ni, respectively. During the subsequent de-lithiation process, the metal particles are re-oxidized to highly disordered nano-sized Fe_2O_3 and NiO particles instead of the original spinel NiFe_2O_4 .

Acknowledgements

This work is sponsored by the Helmholtz Association and the China Scholarship Council.

Reference

- [1] P. Poizot, S. Laruelle, S. Grugeon, L. Dupont, J.M. Tarascon, *Nature* 407 (2000) 496-499.
- [2] R. Alcántara, M. Jaraba, P. Lavela, J.L. Tirado, J.C. Jumas, J. Olivier-Fourcade, *Electrochemistry Communications* 5 (2003) 16-21.
- [3] J. Cabana, L. Monconduit, D. Larcher, M.R. Palacín, *Advanced Materials* 22 (2010) E170-E192.
- [4] J.B. Goodenough, Y. Kim, *Chemistry of Materials* 22 (2010) 587-603.
- [5] G. Zhou, D.-W. Wang, F. Li, L. Zhang, N. Li, Z.-S. Wu, L. Wen, G.Q. Lu, H.-M. Cheng, *Chemistry of Materials* 22 (2010) 5306-5313.
- [6] J. Jiang, Y. Li, J. Liu, X. Huang, C. Yuan, X.W. Lou, *Advanced Materials* 24 (2012) 5166-5180.
- [7] Y.-N. NuLi, Q.-Z. Qin, *Journal of Power Sources* 142 (2005) 292-297.
- [8] R. Kalai Selvan, N. Kalaiselvi, C.O. Augustin, C.H. Doh, C. Sanjeeviraja, *Journal of Power Sources* 157 (2006) 522-527.
- [9] X. Guo, X. Lu, X. Fang, Y. Mao, Z. Wang, L. Chen, X. Xu, H. Yang, Y. Liu, *Electrochemistry Communications* 12 (2010) 847-850.
- [10] P. Lavela, N.A. Kyeremateng, J.L. Tirado, *Materials Chemistry and Physics* 124 (2010) 102-108.
- [11] C. He, S. Wu, N. Zhao, C. Shi, E. Liu, J. Li, *ACS Nano* 7 (2013) 4459-4469.
- [12] A.S. Hameed, H. Bahiraei, M.V. Reddy, M.Z. Shoushtari, J.J. Vittal, C.K. Ong, B.V.R. Chowdari, *ACS Applied Materials & Interfaces* 6 (2014) 10744-10753.
- [13] L. Duan, Y. Wang, L. Wang, F. Zhang, L. Wang, *Materials Research Bulletin* 61 (2015) 195-200.
- [14] S. Permien, S. Indris, M. Scheuermann, U. Schürmann, V. Mereacre, A.K. Powell, L. Kienle, W. Bensch, *Journal of Materials Chemistry A* 3 (2015) 1549-1561.
- [15] M.V. Reddy, C.Y. Quan, K.W. Teo, L.J. Ho, B.V.R. Chowdari, *The Journal of Physical Chemistry C* 119 (2015) 4709-4718.
- [16] S. Permien, S. Indris, A.-L. Hansen, M. Scheuermann, D. Zahn, U. Schürmann, G. Neubüser, L. Kienle, E. Yegudin, W. Bensch, *ACS Applied Materials & Interfaces* 8 (2016) 15320-15332.
- [17] S. Permien, S. Indris, U. Schürmann, L. Kienle, S. Zander, S. Doyle, W. Bensch, *Chemistry of Materials* 28 (2016) 434-444.
- [18] C.T. Cherian, M.V. Reddy, G.V.S. Rao, C.H. Sow, B.V.R. Chowdari, *Journal of Solid State Electrochemistry* 16 (2012) 1823-1832.

- [19] J.-M. Tarascon, S. Grugeon, M. Morcrette, S. Laruelle, P. Rozier, P. Poizot, *Comptes Rendus Chimie* 8 (2005) 9-15.
- [20] D. Bresser, E. Paillard, R. Kloepsch, S. Krueger, M. Fiedler, R. Schmitz, D. Baither, M. Winter, S. Passerini, *Advanced Energy Materials* 3 (2013) 513-523.
- [21] Y. Ding, Y. Yang, H. Shao, *Journal of Power Sources* 244 (2013) 610-613.
- [22] C.T. Cherian, J. Sundaramurthy, M.V. Reddy, P. Suresh Kumar, K. Mani, D. Pliszka, C.H. Sow, S. Ramakrishna, B.V.R. Chowdari, *ACS Applied Materials & Interfaces* 5 (2013) 9957-9963.
- [23] S.D. Kelly, K.M. Kemner, J.B. Fein, D.A. Fowle, M.I. Boyanov, B.A. Bunker, N. Yee, *Geochim. Cosmochim. Acta* 66 (2002) 3855-3871.
- [24] B. Ravel, M. Newville, *Journal of Synchrotron Radiation* 12 (2005) 537-541.
- [25] A.L. Ankudinov, B. Ravel, J.J. Rehr, S.D. Conradson, *Physical Review B* 58 (1998) 7565-7576.
- [26] G. Balachandran, D. Dixon, N. Bramnik, A. Bhaskar, M. Yavuz, L. Pfaffmann, F. Scheiba, S. Mangold, H. Ehrenberg, *ChemElectroChem* 2 (2015) 1510-1518.
- [27] J. Wong, F.W. Lytle, R.P. Messmer, D.H. Maylotte, *Physical Review B* 30 (1984) 5596-5610.
- [28] C.M.B. Henderson, J.M. Charnock, D.A. Plant, *Journal of Physics: Condensed Matter* 19 (2007) 076214.
- [29] M.M. Thackeray, W.I.F. David, J.B. Goodenough, *Materials Research Bulletin* 17 (1982) 785-793.
- [30] C.J. Chen, M. Greenblatt, J.V. Waszczak, *Solid State Ionics* 18-19, Part 2 (1986) 838-846.
- [31] R. Dedryvère, S. Laruelle, S. Grugeon, P. Poizot, D. Gonbeau, J.M. Tarascon, *Chemistry of Materials* 16 (2004) 1056-1061.
- [32] E. Sobczak, N.N. Dorozhkin, *Journal of Alloys and Compounds* 286 (1999) 108-113.
- [33] D. Carta, M.F. Casula, A. Falqui, D. Loche, G. Mountjoy, C. Sangregorio, A. Corrias, *The Journal of Physical Chemistry C* 113 (2009) 8606-8615.
- [34] A.V. Chadwick, *Solid State Ionics* 177 (2006) 2481-2485.
- [35] A.V. Chadwick, S.L.P. Savin, S. Fiddy, R. Alcántara, D. Fernández Lisbona, P. Lavela, G.F. Ortiz, J.L. Tirado, *The Journal of Physical Chemistry C* 111 (2007) 4636-4642.
- [36] S. Permien, H. Hain, M. Scheuermann, S. Mangold, V. Mereacre, A.K. Powell, S. Indris, U. Schurmann, L. Kienle, V. Duppel, S. Harm, W. Bensch, *RSC Advances* 3 (2013) 23001-23014.
- [37] S. Komaba, T. Mikumo, N. Yabuuchi, A. Ogata, H. Yoshida, Y. Yamada, *Journal of The Electrochemical Society* 157 (2010) A60-A65.